URSI GASS 2023, Sapporo, Japan, 19 - 26 August 2023

Calibrated measurements of the EMF enhancement in the downlink of a 6G distributed antenna array testbed

Sergei Shikhantsov*(1), Haolin Li(1), Sam Aerts(2), Olivier Caytan(1),
Guy Torfs(1), Piet Demeester(1), Luc Martens(1), and Wout Joseph(1)
(1) Ghent University/IMEC, Ghent, Belgium; e-mail: sergei.shikhantsov@ugent.be
(2) The Hague University of Applied Sciences, Delft, The Netherlands

Abstract

With this contribution, the results of the measurement campaign performed with a synchronously distributed antenna array testbed operating at the center frequency of 3.686 GHz are presented. For the first time, to the best of the authors' knowledge, the electric field distribution induced by coherent downlink transmission was experimentally assessed in the proximity of the target receiver using a calibrated electromagnetic field probe. This allowed to quantify the actual observed electric field gain and the shape of the electric field enhancement region around the target received. It was found that 16 transmitting antenna elements enhance the root-mean-square electric field level by about a factor of two, in a 2.5λ neighborhood of the target receiver. In addition, a possible disruption of the propagation environment due to the probe movement was assessed through the real-time channel state information feedback.

1 Introduction

Wireless communication systems of the fifth generation (5G) started to employ large antenna arrays at the base station (BS) side, and the number of the antenna array elements is expected to increase in the future [1]. Antenna arrays operating in the Time-Division-Duplex regime use dynamic precoding schemes to boost the electromagnetic field (EMF) level around a target receiver, and thus its received signal strength, based on the wireless channel state communicated by the receiver in the uplink. Currently, numerous measurement campaigns studied the wireless channel properties of such reciprocity-based systems [2–4], based on which key performance characteristics of the wireless link can be derived, e.g., the bit error rate or channel capacity. Contrary to that, not much is known about the actual EMF distribution in proximity of the target receivers. Measurements in [**?**, 5] used channels estimated at a receiver that was attached to a linear actuator to reconstruct the spatial channel correlation function. The correlation function magnitude is proportional to the power received at a particular location, that can be used as a proxy for the EMF strength. One major limitation of this approach is that, as the absolute received power and the receiver antenna factor were not known, only the relative EMF level could be estimated. In addition, this approach is sensitive to the polarization matching between the transmitting and receiving antennas, and thus it does not yield the full vector E-field magnitude.

The paper describes, for the first time, the actual electric field gain in the downlink of a 5G distributed antenna array testbed. A calibrated triaxial EMF probe was used to assess the spatial distribution of the full vector electric field root-mean-square (E_{RMS}) magnitude around the receiver location with a sub-wavelength spatial resolution.

2 Experimental setup

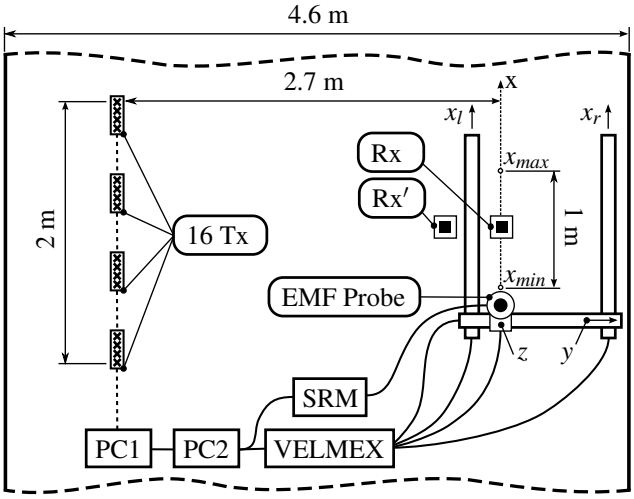

Figure 1. Top view of the measurement setup (to scale). The 'PC1', 'PC2', 'SRM' and 'VELMEX' blocks schematically depict the testbed control PC, the probe/actuator control PC, the dedicated probe and the actuator control hardware, respectively, together with their interconnections.

2.1 Setup description

The top view of the experimental setup is schematically shown in Fig. 1. The testbed consists of 16 transmitter (Tx) antenna elements arranged in four sub-arrays of four elements each, in a straight line at the height of around 1.5 m, as indicated in Fig. 1 with black crosses. The inter-element distance in the sub-arrays is 65 mm, and the distance between the sub-arrays' centers is 450 mm. This results in a

Data bandwidth	46.09 MHz
FFT size	128
Sub-carrier number	128
Sub-carrier spacing	360.1 kHz
Cyclic prefix size	32

Table 1. OFDM signal parameters.

total Tx array span of around 2 m. A single receiving (Rx) antenna element was positioned at the same distance from the ground and at the shortest distance from the Tx array line of around 2.7 m (as indicated in Fig. 1 as 'Rx'). Both Tx and Rx elements are wideband single-element substrate integrated waveguide cavity-backed slot antennas with a gain of 5.4 dBi at 3.686 GHz [6]. The Tx-Rx system continuously transmits the OFDM signals, the parameters of which are summarized in Table 1, at the center frequency of 3.686 GHz. It is controlled from PC1, which is schematically shown in Fig. 1 with a rectangle. All the remotely distributed antennas are connected in a synchronous manner to the centralized unit on the PC1 via multi-mode fibers. The tight phase synchronization among these antennas is guaranteed by extracting the clock from the data on fiber [7].

In addition, a motorized 3D Cartesian actuator (VELMEX) was placed in proximity of the Rx antenna. The actuator had a wideband (900 MHz-6 GHz) triaxial EMF probe attached to its moving arm, shown with the circle in Fig. 1. The probe was connected to the Narda SRM-3006 field strength analyzer, shown with the rectangle in Fig. 1 and is further referred to as the SRM. The actuator and the SRM were remotely operated from PC2. The PC1 and PC2 were interconnected via the BSD Socket interface (over Ethernet, using the TCP protocol), which allowed for the coordinated control of the testbed, the probe positioning, and the measured EMF level acquisition.

2.2 Experiments

With the EMF probe at the initial position (depicted in Fig. 1 as 'Rx'), the channel vector to the single Rx antenna $\mathbf{h} \in \mathbb{C}^{16\times128}$ was estimated, where the first dimension ($m = 16$) tracks the Tx element index, and the second ($n = 128$) - the sub-carrier index. Three experiments were conducted:

1) The first experiment assesses the EMF distribution around the initial Rx location while the Tx array targets that location with the Maximum Ratio Transmission (MRT) precoding by applying the transmit weights $\mathbf{t} \in \mathbb{C}^{16\times128}$. The Rx antenna itself is removed from its initial location to allow the EMF probe to move freely along the straight line for a total distance of 1 m (depicted as the dashed line in Fig. 1, the x-axis). The y-coordinate of the EMF probe coincides with the y-coordinate of the Rx antenna's initial location during this experiment. Four 1D-scans along the x-axis were performed, at the EMF probe center z-offsets of -100 mm, 0 mm (coincident), 100 mm, and 200 mm relative to the Rx antenna center z-coordinate. Furthermore, one additional 1D-scan with 0 mm z-offset was performed with the Tx transmission turned off in order to obtain the background EMF level.

2) The second experiment assesses the baseline to which the MRT EMF enhancement is compared to. To establish this baseline, the initial transmit weights vector $\mathbf{t}$ is altered ('scrambled') by multiplying each of its elements with a pseudo-random complex number μ, sampled from a uniform distribution on the complex unit circle, i.e. $\mu = e^{i\varphi}$, where φ is distributed uniformly in $(0, 2\pi)$. Multiplying the transmit weights by μ randomly shifts the phase of each Tx element, fully decorrelating the resulting transmission. Six 1D-scans as above are performed repeatedly, each with an independently selected set of the phase-shifts μ.

3) The third experiment assesses the channel variation due to the EMF probe and the actuator movement in the measurement process. The Rx antenna is kept stationary at the location indicated as Rx$'$ in Fig. 1, such that the EMF probe is able to travel along the same track as in the first two experiments (now in proximity to the Rx's new position). At each stationary position of the probe x_i, the Tx estimates the channel vector $\mathbf{h}_i(f_n)$. This is done for seven equidistant locations of the probe along the 600 mm section of the x-axis (with a 100 mm step), centered with respect to the x-coordinate of the Rx$'$. The difference between the channel vector estimates $\mathbf{h}_i(f_n)$ indicates the amount of channel variation resulting from the probe movement. However, no EMF is measured in this experiment.

3 Results and discussion

3.1 Spectrum

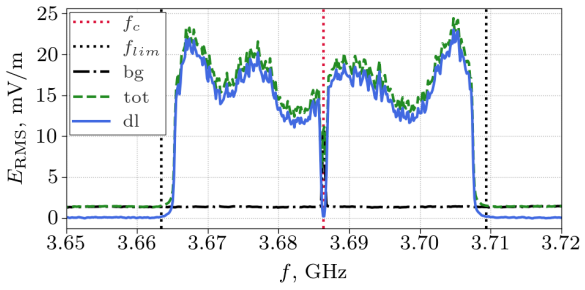

Figure 2. The measured spectrum at the starting position of the EMF probe ($x = 0$). The dashed green line shows the total EMF strength (in terms of the RMS electric-field strength) in the bandwidth occupied by the channel (Tx on), while the black dash-dotted line shows the background E_{RMS} level (Tx off), and the solid blue line shows the difference of the two (the downlink signal). The dotted black and red lines show the band limits and center, respectively.

The dashed green line in Fig. 2 shows the E_{RMS} spectrum

measured with the Tx transmitting random symbols precoded using the MRT scheme based on the channel estimated with the Rx at its initial location (indicated as Rx in Fig. 1). The dash-dotted black line in Fig. 2 shows the background E_{RMS} spectrum measured with the Tx off at the same position of the EMF probe. Each point in Fig. 2 is an integral of the E_{RMS} spectral density over the resolution bandwidth interval of the SRM ($\approx$ 156 kHz). The solid blue line in Fig. 2 shows the difference of the two, which is taken to be the downlink E_{RMS} spectrum.

The E_{RMS} contribution outside the Tx band of 3.686 ± 0.023 GHz (delimited with two vertical black dotted lines in Fig. 2) is negligibly small compared to the in-band signal. A relatively low E_{RMS} level around f_c (marked with the dotted red vertical line in Fig. 2) results from the three OFDM DC sub-carriers at the center of the band (about 1.08 MHz wide) [7].

3.2 E_{RMS} spatial distribution

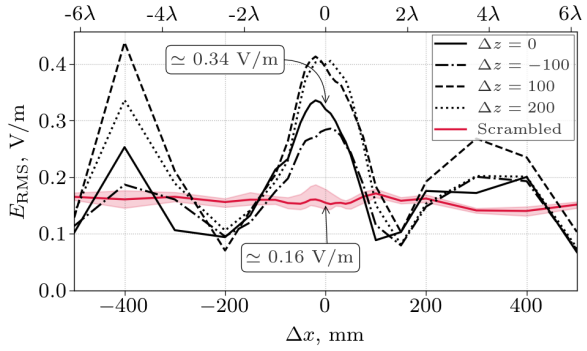

Figure 3. The E_{RMS} variation along the x-axis (see Fig. 1). The black color lines show the MRT-precoded E_{RMS} for different z-offsets. The solid red line shows the average E_{RMS} with scrambled channels (no precoding), and the shaded region around it shows the E_{RMS} variation across six measurement runs.

The in-band integral of the Tx-induced E_{RMS} is calculated at every position of the probe in several scenarios shown in Fig. 3. Fig. 3 shows that in each of the four 1D-scans, the E_{RMS} maximum is observed at the probe x-coordinate coinciding with the Rx ($\Delta x = 0$). This is expected, as the linear array radiation pattern is selective in azimuth and largely uniform in elevation. In addition, two auxiliary local maxima at $\Delta x \simeq \pm 4\lambda$ are seen. These are induced by the grating lobes of the array pattern, resulting from the sub-array separation distance significantly exceeding one wavelength. Interestingly, the highest E_{RMS} of around 0.4 V/m at $\Delta x = 0$ is observed at 100 mm and 200 mm above the Rx position ($\Delta z = 100$ and 200 - the dashed and dotted lines in Fig. 3). This is likely caused by reflections in the environment, e.g., back-scattering from the wall opposite to the Rx location (see Fig. 1). The E_{RMS} observed with the scrambled channels (red line and shaded region in Fig. 3) is nearly constant across the entire x-axis span of 1 m and equals around 0.16 V/m. The E_{RMS} enhancement region cross-section size is calculated as the distance between the two points at which the MRT-precoded E_{RMS} falls down to the scrambled E_{RMS} level. It is estimated to be just over 200 mm (2.5λ), which is around half of the estimate in [5]. This is likely due to the increased aperture of the distributed linear Tx array (relative to the wavelength), compared to the collocated planar array in [5].

With this, the E_{RMS} array gain $G \simeq 2$ is calculated as the ratio between the peak E_{RMS} ($\simeq$ 0.34 V/m, as observed at the Rx location, $\Delta z = 0$) and the average E_{RMS} value observed with scrambled channels at the same location. This is around twice lower than the theoretical maximum E_{RMS} MRT gain [8] $G_{max} = 4$ for a MIMO system with 16 Tx elements. One of the possible reasons for this is an imperfect phase synchronization between the Tx elements, caused by phase noise/jitter and quantified in [7]. Another - the EMF probe movement between the measurement positions violating the channel stationarity condition, assessed in the third experiment, the results of which are discussed below.

3.3 Channel correlation

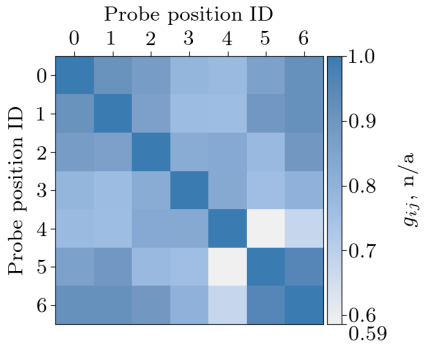

Figure 4. The correlation matrix of the Rx channel vectors with the EMF probe at different locations.

As noted above, changing the EMF probe position alters the wireless channel. Fixing the channel estimated at the initial probe position for the whole duration of the first experiment sets the constant transmit weights that maximize the Rx power, i.e. moving the probe in proximity of the Rx location reduces the MRT gain at that position. To quantify this effect, the channel correlation function

$$g_{ij} = \frac{1}{128} \sum_{n=1}^{128} |(\bar{\mathbf{h}}_i(f_n), \bar{\mathbf{h}}_j(f_n))|, \qquad (1)$$

i.e. the sub-carrier average of the normalized channel vectors' pair-wise inner product is calculated at every position of the probe in the third experiment. In (1), $\bar{\mathbf{h}}_i(f_n)$ are $\mathbf{h}_i(f_n)$ normalized, such that $g_{ii} = 1$, $\forall i$. Thus, $g_{ij} = 1$ for $\bar{\mathbf{h}}_i$ and

$\bar{\mathbf{h}}_j$ spanning the same linear channel subspace for all subcarriers, and $g_{ij} = 0$ for strictly orthogonal $\bar{\mathbf{h}}_i$ and $\bar{\mathbf{h}}_j$. The values of g_{ij} for $i, j \in [0, 6]$ are shown in Fig. 4.

The g_{ij} values in the central row ($i = 3$, or $\Delta x = 0$) do not fall below 0.75, meaning that the E_{RMS} measured at the Rx location is at most 25% below its actual value. This puts the upper bound on the amount of channel decorrelation caused by the probe, assuming this effect is equivalent for Rx$'$ and the initial Rx position. Overall, g_{45} has the lowest value of around 0.6. Generally, higher g_{ij} in the top-left and bottom-right corners of in Fig. 4 indicate that the probe movement further away from the Rx cause less channel decorrelation.

4 Conclusions

This contribution presented the first direct calibrated measurements of the EMF enhancement in downlink of a synchronous distributed antenna system. The average E-field gain of around 2 was experimentally obtained, and the size of the enhancement region was estimated at around 2.5λ with 16 Tx antenna elements. The inherent accuracy limitation of the presented method was assessed with real-time channel measurements.

Acknowledgements

This work was supported by the ERC Advanced Grant ATTO (No. 695495), EU H2020 ERC-POC BI-SDMoF (No. 839200), EU H2020 Int5Gent (No. 957403) project, and Methusalem SHAPE: Next Generation Wireless Networks. Sergei Shikhantsov is a postdoctoral fellow of the Special Research Fund (BOF).

References

[1] E. Björnson, L. Sanguinetti, H. Wymeersch, J. Hoydis, and T. L. Marzetta, "Massive MIMO is a reality-what is next?: Five promising research directions for antenna arrays," *Digital Signal Processing*, vol. 94, pp. 3 – 20, 2019, special Issue on Source Localization in Massive MIMO.

[2] A. Karstensen, J. Ø. Nielsen, P. Eggers, E. De Carvalho, M. Alm, and G. Steinböck, "Dual-user massive MIMO measurements at 3.5 GHz with bi-directional angular discrimination," in *2018 12th European Conference on Antennas and Propagation (eucap)*, 2018.

[3] X. Gao, O. Edfors, F. Rusek, and F. Tufvesson, "Massive MIMO performance evaluation based on measured propagation data." *IEEE Trans. Wireless Communications*, vol. 14, no. 7, pp. 3899–3911, 2015.

[4] S. Claessens, C.-M. Chen, D. Schreurs, and S. Pollin, "Massive MIMO for SWIPT: A measurement-based study of precoding," in *2018 IEEE 19th International Workshop on Signal Processing Advances in Wireless Communications (SPAWC)*, 2018, pp. 1–5.

[5] S. Shikhantsov, A. Guevara, A. Thielens, G. Vermeeren, P. Demeester, L. Martens, G. Torfs, S. Pollin, and W. Joseph, "Spatial correlation in indoor massive mimo: Measurements and ray-tracing," *IEEE Antennas and Wireless Propagation Letters*, 2021.

[6] S. Lemey, O. Caytan, D. V. Ginste, P. Demeester, H. Rogier, and M. Bozzi, "SIW cavity-backed slot (multi-)antenna systems for the next generation IoT applications," in *2016 IEEE Topical Conference on Wireless Sensors and Sensor Networks (WiSNet)*, 2016, pp. 75–77.

[7] C.-Y. Wu, H. Li, J. Van Kerrebrouck, C. Meysmans, P. Demeester, and G. Torfs, "A bit-interleaved sigma-delta-over-fiber fronthaul network for frequency-synchronous distributed antenna systems," *Applied Sciences*, vol. 11, no. 23, p. 11471, 2021.

[8] E. Björnson, J. Hoydis, and L. Sanguinetti, "Massive MIMO networks: Spectral, energy, and hardware efficiency," *Foundations and Trends in Signal Processing*, vol. 11, no. 3-4, pp. 154–655, 2017.